HYDRODYNAMIC STUDY OF SIX ROWING BLADES USING MULTI-LAYER PLANAR PIV

Shanwei Zhou, Arnoud J. Greidanus, Jerry Westerweel and Mark J. Tummers
Laboratory for Aero & Hydrodynamics
Delft University of Technology
Mekelweg 2, 2628 CD, Delft, The Netherlands
S.Zhou-2@tudelft.nl

ABSTRACT
This study investigates the hydrodynamic performance of six rowing blades using force measurements and multi-layer planar particle image velocimetry (PIV) measurements. The results show that leading-edge and trailing-edge-vortices dominate both flow behavior and propulsion at different phases of a rowing stroke. A 3D impulse-based method is applied to the PIV data and shown to reconstruct the hydrodynamic forces with good agreement to force measurements. The results of this study highlight the key role of vortices to rowing propulsion and provide insights for improving blade design and rowing efficiency.

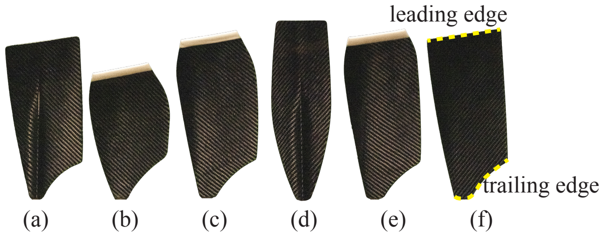

Figure 1. Models of the rowing blades for sculling considered in this research: (a) Big blade, (b) Comp blade, (c) Fat2 blade, (d) Macon blade, (e) Smoothie2 Vortex Edge blade, and (f) the Smoothie2 Plain Edge blade. The definition of the leading edge and the trailing edge is illustrated in (f).

INTRODUCTION
In competitive rowing, performance differences between teams are often less than one second over a 2000 m race. Therefore small improvements in the propulsion efficiency of the rowing blades may have a large impact on the race outcome. The hydrodynamics of rowing propulsion have been investigated in several studies. In particular, Grift *et al.* (2021) combined force measurements and particle image velocimetry (PIV) measurements to demonstrate that blade forces are strongly governed by blade kinematics and blade–fluid interaction. Three-dimensional flow structures around a blade have been explored numerically by Coppel *et al.* (2010) for fixed angles of attack. Apart from this, van Nieuwburg *et al.* (2023) used a robotic rowing boat model in a towing tank to investigate propulsion efficiency under equal power conditions. Other studies have focused on the relationship between stroke parameters, blade forces, and efficiency, see Kleshnev (2026); Caplan & Gardner (2007); Baudouin & Hawkins (2004). However, these approaches provide limited insight into the time-resolved flow structures underlying force generation during a rowing stroke. Rowing propulsion is inherently unsteady and dominated by vortex dynamics, including leading-edge and trailing-edge vortices and the resulting wake. Eldredge & Jones (2019) show that such structures are playing a key role in force generation in related drag-based propulsion systems. However, their spatial and temporal evolution in rowing remains insufficiently resolved.

The objective of this study is to determine the relationship between flow structures and hydrodynamic forces in rowing blades during different phases of a stroke. Six blades are investigated using time-resolved force measurements and multi-layer planar PIV measurements. A semi-time-resolved 3D flow field is reconstructed, and a 3D impulse-based method is applied to directly link flow structures to the generated hydrodynamic forces.

EXPERIMENTAL SET-UP
Blade Models and Blade Tip Path
A front view of the six blade models is shown in Figure 1. Note that Figure 1 (f) is used to define the leading and trailing edges of the blades. The six rowing blades are 3D scanned and then scaled down by a factor of 1:1.6 to match the Big blade model used by Grift *et al.* (2021). The blade models are manufactured using stereo-lithography 3D printing and subsequently laminated with carbon fiber to replicate the stiffness of the full-scale blades. A clear coat is applied to reproduce the original surface roughness.

A schematic of the experimental setup used in this study is shown in Figure 2. To perform the force and PIV measurements, the rowing blade models are mounted on a gantry robot (Reis Robotics RL50). The blades are moved through water in an open-top glass tank with dimensions $2.0\,\mathrm{m} \times 2.0\,\mathrm{m} \times 0.6\,\mathrm{m}$, which is filled with water up to a height of 0.5 m. The blades follow the same blade tip path and velocity profile as described by Grift *et al.* (2021). During a rowing stroke, the top of the blade is submerged to a depth of $H = 70\,\mathrm{mm}$ below the free-surface of water. As shown in Figure 2, the coordinate system used in this experiment has the origin of the $x-$ and $y-$axes at the starting point of the stroke. The origin of the $z-$axes is at the highest point of the blade in the middle the stroke. Figure 3 illustrates the decomposition of the resulting hydrodynamic force F acting on the blade into components F_x, F_y in the $x,y-$coordinate system and components F_n, F_t in the

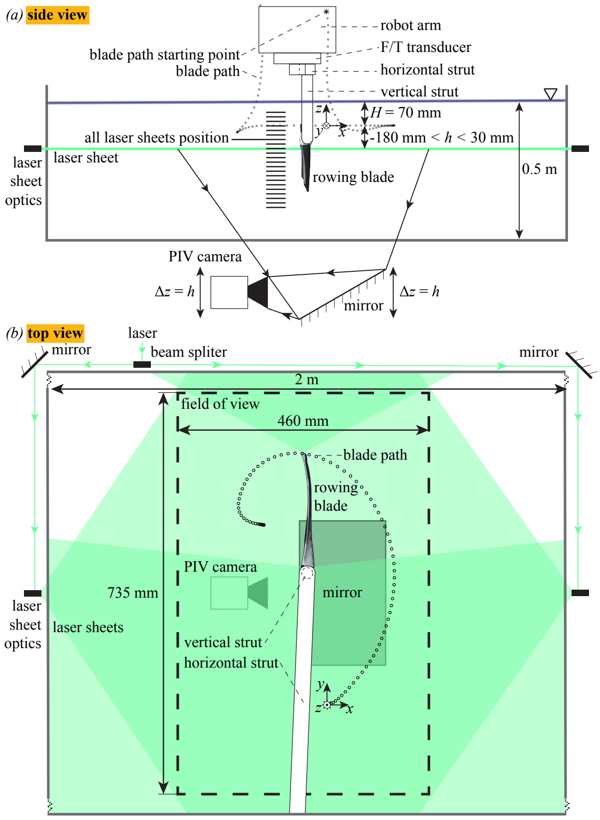

Figure 2. Schematic of experimental set-up. (a) A side view of the experimental set-up. In the top view (b), every object inside the rectangle box marked by the dashed line has been scaled up by a factor of two. Corresponding objects in the side view follow the same scale.

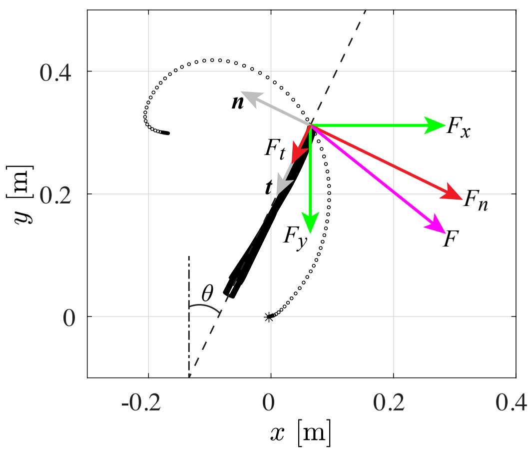

Figure 3. Decomposition of the hydrodynamic force F. The angle between the rowing blade chord and the $y-$axis is given by θ.

$n,t-$coordinate system, where n and t are in directions normal to the chord and parallel to the chord, respectively.

Hydrodynamic force and PIV Measurements

See Figure 2, to measure the hydrodynamic force, the blades are attached to an ATI 6 DOF force/torque transducer taking samples at a rate of 10 kHz. To measure the flow field, a PIV camera (Phantom VEO 640L) is positioned beneath the tank, oriented horizontally and viewing vertically upward through a 30° mirror. It captures images consisting 2560×1600 pixels at 1487 frames per second (fps) over a $460\,\text{mm} \times 735\,\text{mm}$ field of view. Neutrally buoyant fluorescent tracer particles (Cospheric UVPMS-BR-1.03) with diameters in the range of 105–125 μm are added to the water. Illumination of the particles is provided by two overlapping horizontal laser sheets coming from opposing sides, thus minimizing shadows cast by the opaque blade model. The laser light sheets are generated by a dual-cavity Nd:YLF laser (Litron LD30-527 PIV), a beam splitter and two sets of light sheet optics. DaVis 10.2 (LaVision GmbH) is used for the images acquisition. The images are then processed using an in-house developed MATLAB script based on the PIV methods described by Adrian & Westerweel (2011).

During the PIV measurements, the flow fields at various heights around the blades are captured. The top edge of the blade during the stroke is defined as the reference height, $h = 0\,\text{mm}$, see Figure 2 (a). In total, eleven different planes are recorded, ranging from 30 mm above the top of the blade ($h = 30\,\text{mm}$) to 180 mm below the top of the blade ($h = -180\,\text{mm}$).

HYDRODYNAMIC FORCE MEASUREMENT RESULTS

Figure 4 shows the results of the hydrodynamic force measurements for the six rowing blades. F_n is the force component normal to the blade chord and t^* is the dimensionless time defined as $t^* = (t - t_{\text{catch}})/(t_{\text{release}} - t_{\text{catch}})$, where t_{catch} denotes the moment of the blade being fully submerged, and t_{release} marks the moment when the top of the blade reaches the free surface. It is important to note that, due to this definition, the blade remains in the water slightly beyond $t^* = 1$ and one of the peaks in the normal force component F_n often occurs during this extended period.

As shown in Figure 4, most blades exhibit similar force behavior throughout the stroke. The positions of the force peaks and valleys largely coincide for all blades, except for the Comp blade (in red), which displays two distinct peaks around $t^* = 0.5$, rather than a single peak. There are still some minor differences among the hydrodynamic forces for other rowing blades. For example, a slight phase shift of the normal force component F_n for $t^* < 0.25$ and $t^* > 0.75$ can be observed. This phase shift is characterized by the relative timing of the catch valleys and release peaks: the catch valley refers to the first valley after $t^* = 0$, and the release peak denotes the first peak following $t^* = 1$.

PIV MEASUREMENT RESULTS

Time-Resolved PIV Measurement Results

To gain a deeper understanding of the differences in force behavior, PIV measurements are conducted for all the rowing blades during a stroke. The inset in Figure 4 shows four snapshots of the flow field for the Smoothie2 Plain Edge blade between $t^* = 0.2$ and $t^* = 1.1$ at height $h = -60\,\text{mm}$. The streamlines are indicated by black arrowed lines while the colors represent the out-of-plane component of the vorticity (ω_z). The blade tip path is shown as gray dashed lines in Figure 4 (a)–(d) and in Figure 5, with the blade position at a specific moment indicated by a thick black line.

At $t^* = 0.2$, both the leading edge vortex (LEV) and the initial trailing edge vortex (TEV) are formed. The fluid in front of the blade is displaced by the blade motion. A characteristic shear flow is evident near both the leading and trailing edges, as indicated by the streamlines that are not perpendicular to

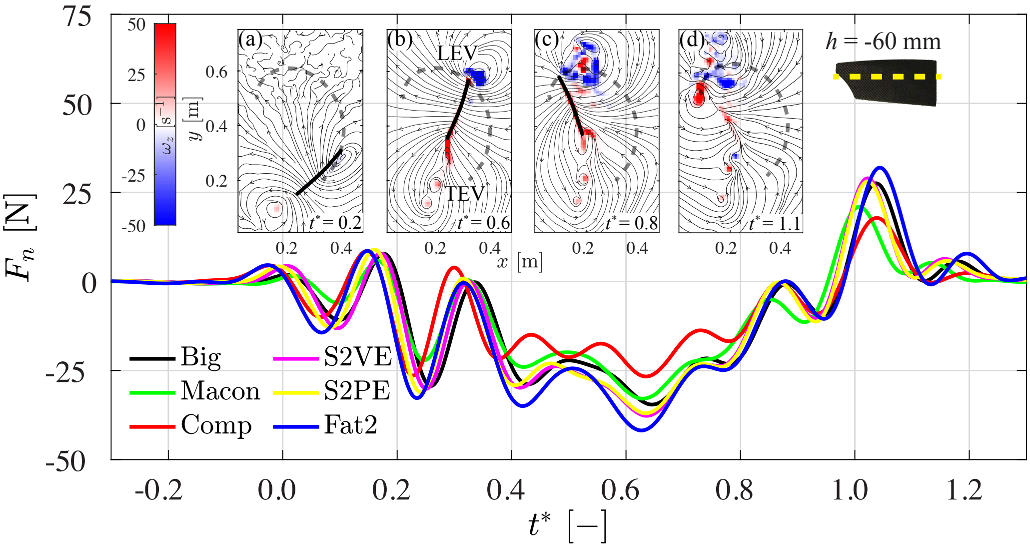

Figure 4. A comparison of the normal force component F_n for six rowing blades as a function of the dimensionless time t^*. The inset shows instantaneous vorticity fields and streamlines during a rowing stroke at (a) $t^* = 0.2$, (b) $t^* = 0.6$, (c) $t^* = 0.8$ and (d) $t^* = 1.1$, for the Smoothie2 Plain Edge blade at height $h = -60$ mm.

the blade surface. The fluid located at $y < 0.5$ m is still largely unaffected by the blade motion.

At $t^* = 0.6$, the second and thirds TEVs are generated. The LEV remains attached to the back of the blade and increases in strength. Strong shear flow continues to be observed, particularly near the leading and trailing edges, as indicated by the streamline patterns.

At $t^* = 0.8$, a fourth TEV is shed, and the third TEV starts interacting with the back surface of the blade. The LEV detaches from the leading edge and evolves into a turbulent wake region behind the leading edge of the blade.

At $t^* = 1.1$, a pair of opposing vortices is observed around the previous location of the leading edge of the blade. The fluid previously in front of the blade is inverted by the release of the blade. Around the previous location of the trailing edge of the blade, an extra TEV with negative vorticity is formed.

Multi-layer PIV Measurement Results

The flow around the blade is fully three-dimensional throughout the stroke. Therefore, the results of the planar PIV measurement in a single layer at the blade's mid-span (at height $h = -60$ mm) may not be representative for the flow field around the blade. To gain insight into the three-dimensional flow field, multi-layer planar PIV measurements are conducted for the Smoothie2 Plain Edge blade. A typical result from the multi-layer planar PIV measurements at $t^* = 0.8$ is shown in Figure 5. The yellow dashed lines in the bottom-right corner of Figure 5 (a)–(d) indicate four representative measurement planes obtained by adjusting the laser sheet height relative to the blade. By comparing the flow fields at different measurement planes, clear differences in the structure of the LEV, the TEV, and the wake region are observed.

At height $h = -100$ mm, the flow field resembles that measured at height $h = -60$ mm. Even though the size of the LEV is smaller for the former. Also, for $h = -100$ mm, a larger turbulent wake region extends from the LEV to the initial TEV, contained within the area bounded by the blade's extension line and the blade tip path.

At $h = -20$ mm and $h = -140$ mm, the turbulent wake region exhibits higher vorticity magnitude. However, the size

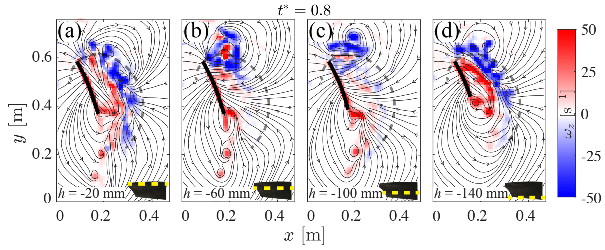

Figure 5. Instantaneous vorticity field and streamlines for the Smoothie2 Plain Edge blade at $t^* = 0.8$ at different measurement heights (a) $h = -20$ mm, (b) $h = -60$ mm, (c) $h = -100$ mm and (d) $h = -140$ mm. The blade position is indicated by thick black solid lines; and the blade tip path is shown as gray dashed lines.

of the wake region is smaller than that for $h = -100$ mm. Most of the vorticity structures remain confined within the blade tip path, with the exception of the shedding LEV, which crosses it. The turbulent wake region at $h = -140$ mm has a smaller size than that at $h = -20$ mm. In addition, at $h = -140$ mm, the TEVs that can be seen in Figure 5 (a), (b) and (c) are not clearly identifiable.

These results from the multi-layer planar PIV measurements highlight the significant variation in flow structures across different measurement planes. Nonetheless, a symmetric-like pattern is observed from the top to the bottom of the blade, suggesting a degree of vertical symmetry in the overall flow field, which will be further discussed in Figures 6 and 7.

3D Flow Reconstruction

Using the results of the multi-layer planar PIV measurement, the third component of velocity vector w can be reconstructed from a modified continuity equation for incompressible flow,

$$w = -\int \left(\frac{\partial u}{\partial x} + \frac{\partial v}{\partial y} \right) \mathrm{d}z. \quad (1)$$

In this study, the iso-surface of the quantity Q introduced by Jeong & Hussain (1995) is chosen to visualize the vortical structures in the reconstructed 3D flow field. A typical result for the Smoothie2 Plain Edge blade is shown by the iso-surface of $Q = 1 \times 10^{-5}\,\mathrm{s}^{-2}$ in the insets of Figures 6 and 7. Since the flow fields for the other blades are comparable with the Smoothie2 Plain Edge blade, only the flow field for the Smoothie2 Plain Edge blade will be discussed here.

Before $t^* = 0.2$, a vortical structure is first generated at the bottom and the trailing edge of the blade, see Figure 6 (a) and (b). As shown in Figure 6 (c), the first TEV detaches from the blade at $t^* = 0.2$. As the rowing stroke moves to $t^* = 0.3$, a clear vortex loop is formed, from the top edge, through the leading edge, to the bottom edge of the blade. Meanwhile, the second TEV detaches from the blade, see Figure 6 (d).

At $t^* = 0.55$, as shown in Figure 7 (a), the LEV, labeled as I, has a curved shape, with the middle of the LEV being detached from the blade. The first and second TEVs have already detached, while the third TEV is being formed. At $t^* = 0.75$, as shown in Figure 7 (b), the LEV is dissipating and developing into a wake region behind the blade. The fourth TEV is formed with the third TEV detached from the blade. At $t^* = 0.9$ and $t^* = 0.95$, as shown in Figure 7 (c) and (d), the initial LEV is fully developed into a turbulent wake region, while a secondary LEV, labeled as II, is formed in front of the blade. Same as the secondary LEV, the fourth TEV is transferred to the front of the blade. At $t^* = 0.95$, the start of release motion increased the strength of the fourth TEV.

These results from the 3D flow reconstruction visualize the development of the 3D vortical structures for the Smoothie2 Plain Edge blade during a rowing stroke. The vortical structures show a high degree of vertical symmetry in the flow field close to the leading edge of the blade. Around the trailing edge of the blade, the vortical structures are non-symmetry and follow the geometry of the trailing edge of the blade

HYDRODYNAMIC FORCE RECONSTRUCTION

3D Impulse-based Method

In this study a 3D impulse-based method to is used reconstruct the hydrodynamic force. The focus will be on the reconstruction of the propulsion force F_x. But in principle, the other components of the hydrodynamic force can also be reconstructed. The 3D impulse-based method is developed from the 2D impulse based method introduced by Gehlert *et al.* (2023):

$$F_{x_{2D}} = \rho \int_R \frac{\mathrm{d}I_x}{\mathrm{d}t}\mathrm{d}R, \tag{2}$$

where R is the 2D region containing the vorticity generated by the object of interest and I_x is the impulse given by:

$$I_x = x\omega_z, \tag{3}$$

where ω_z denotes the vorticity component in the out-of-plane (z) direction. The 3D impulse-based method, is developed by integrating the 2D impulse-based method in the out-of-plane direction:

$$F_x = \int_z \rho \int_R \frac{\mathrm{d}I_x}{\mathrm{d}t}\mathrm{d}R\mathrm{d}z = \int_z F_{x_{2D}}\mathrm{d}z. \tag{4}$$

Using the multi-layer planar PIV measurement data, the 3D impulse-based method can be converted into:

$$F_x = \sum_{i=1}^{n} F_{x_{2D_i}} \Delta z, \tag{5}$$

where n is the number of measured PIV layers and Δz is the distance between the measured layers.

The 3D impulss-based method can also give a space-resolved force reconstruction result, by evaluating the hydrodynamic force contribution at the level of each PIV resolution element. This is done by rewriting Equation 2 as:

$$f_{x_{2D_{ijk}}} = \rho \frac{\mathrm{d}I_{x_{ijk}}}{\mathrm{d}t}, \tag{6}$$

where i is the index in $z-$direction, j is the index in $x-$direction, and k is the index in $y-$direction. Then Equation 4 can be rewritten as:

$$F_x = \iiint_{R_{3D}} f_{x_{2D_{ijk}}} \mathrm{d}R_{3D}, \tag{7}$$

where R_{3D} is the 3D region containing the vorticity generated by the object of interest. The reconstructed local propulsion force contribution is visualized in the insets of Figures 6 and 7, by coloring the iso-surface of Q.

Hydrodynamic force Reconstruction Results

Using Equation 4, the 3D flow field can be used to provide insight into the local flow contribution to the generation of the hydrodynamic force. As shown in Figures 6 and 7, the reconstructed propulsion force F_x (in black) agrees well with the propulsion force measured by the F/T transducer (in green).

It can be observed from the force budget that the flow in the middle ($-120\,\mathrm{mm} < h \leq -40\,\mathrm{mm}$, in cyan) of the blade generates most of the propulsion force between $t^* = 0.2$ and $t^* = 0.6$, while the propulsion force before $t^* = 0.2$ is dominated by the flow at the bottom ($-180\,\mathrm{mm} < h \leq -120\,\mathrm{mm}$, in blue) of the blade. From $t^* = 0.6$ to $t^* = 0.7$, the propulsion force decreases, mainly due to the decrease of propulsion force generated by the flow in the middle of the blade, with the flow at the top of the blade generating a constant level of propulsion force. From $t^* = 0.7$ to $t^* = 0.9$, several peaks and valleys are observed in the measured propulsion force. These are all dominated by the flow in the middle of the blade. After $t^* = 0.9$, the flow at the bottom of the blade dominates the propulsion force generation.

Apart from the time-resolved propulsion force budget, the spatial propulsion force distributions shown in the insets of Figures 6 and 7 give more detailed information about the source of the propulsion force generation. This information may lead to insights relevant to improving the design of rowing blades.

At $t^* = 0.10$, a peak in the propulsion force is observed, which is generated by the vortex loop from the bottom edge to the trailing edge of the blade, labeled by II in Figure 6 (a). Apart from that, the vorticity generated by the holding structure of the blade, labeled by I, also contributes to the propulsion force.

A valley is observed in the propulsion force at $t^* = 0.13$. Labeled by I & II in Figure 6 (b), the vortical structures that

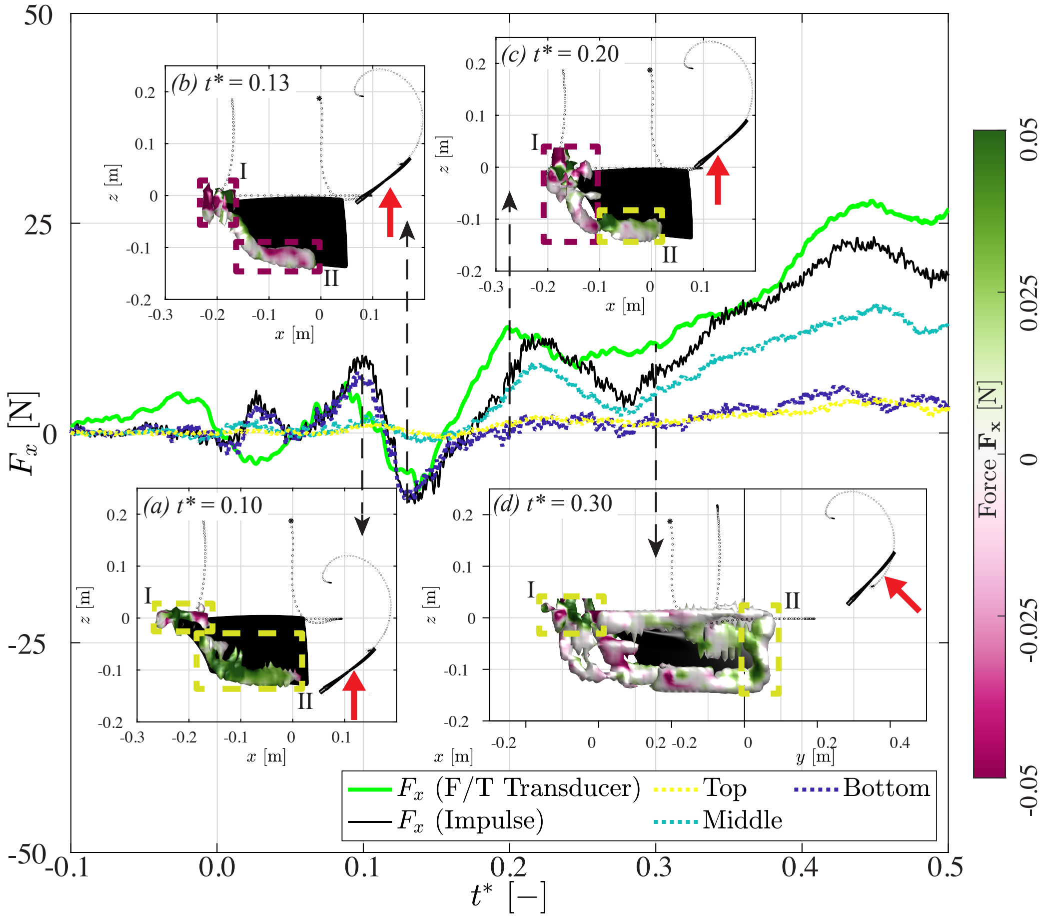

Figure 6. The propulsion force F_x for the Smoothie2 Plain Edge blade as a function of dimensionless time t^* during the first half of the stroke between $t^* = -0.1$ and $t^* = 0.5$. The propulsion force measured by the F/T transducer is shown in green. The propulsion force reconstructed from the multi-layer impulse-based method is shown in black, with the force budget reconstructed from the flow at the top, middle and bottom of the blade is shown in yellow, cyan and blue, respectively. The insets at (a) $t^* = 0.10$, (b) $t^* = 0.13$, (c) $t^* = 0.20$ and (d) $t^* = 0.30$ show the iso-surface of $Q = 1 \times 10^{-5}\,\mathrm{s}^{-2}$ and the color represents the local contribution of propulsion force F_x. The main flow structure contributing to the propulsion force is marked by dashed rectangles and labeled by roman numerals I and II. Inside of each inset, the viewing angle is indicated by a red arrow pointing at the top view of the blade at the same t^*.

previously (at $t^* = 0.10$) generated positive propulsion force, now generate negative propulsion force. It is specular here that this difference could be caused by the elastic deformation and recovery of the rowing blade, which contributes to the instability in the strength of the generated vortical structures.

For the same reason, another peak in propulsion force is observed at $t^* = 0.20$. As shown in Figure 6 (c), the detached TEV (labeled by I) generates negative propulsion force, while the vortex generated from the bottom edge, but close to the trailing edge (labeled by II) generates positive propulsion force and balances out the negative propulsion force generated by the detached TEV.

At $t^* = 0.30$, the propulsion force is steadily increasing. As shown in Figure 6 (d), the LEV (labeled by II) is generated, and contributes strongly to the positive propulsion force, while the holding structure (labeled by I) also generates positive propulsion force. Due to the contribution from the enhancing LEV, the propulsion force is increasing until reaching a global maximum at $t^* = 0.55$, as shown in Figure 7 (a). During this phase, the TEVs are detaching from the blade while generating positive propulsion force.

A valley in propulsion force occurs at $t^* = 0.75$. As shown in Figure 7 (b), the LEV develops into a turbulent wake region (labeled by II), but still generates net positive propulsion force. The general propulsion force turns negative, due to the formation of the vortical structure in front of the blade (labeled by II).

At $t^* = 0.90$, the propulsion force reaches a global minimum. As shown in Figure 7 (c), the negative propulsion force is mainly generated by the secondary LEV labeled by II, while the wake region developed from the initial LEV still generates positive propulsion force.

Between $t^* = 0.90$ and $t^* = 0.95$ the propulsion force recovers. As shown in Figure 7 (d), the TEV generated in front of the blade (labeled by III) has a positive contribution to the propulsion force, while the secondary LEV labeled by II detaches from the blade, and generates less negative propulsion force.

CONCLUSION

Hydrodynamic forces were measured using a force/torque transducer, while planar particle image velocimetry (PIV) measurements were performed for six different rowing blades translated through water along a realistic blade path by a gantry robot. Planar PIV data were acquired in 11 horizontal planes at varying heights relative to the blade. These measurements were subsequently used to reconstruct the third velocity

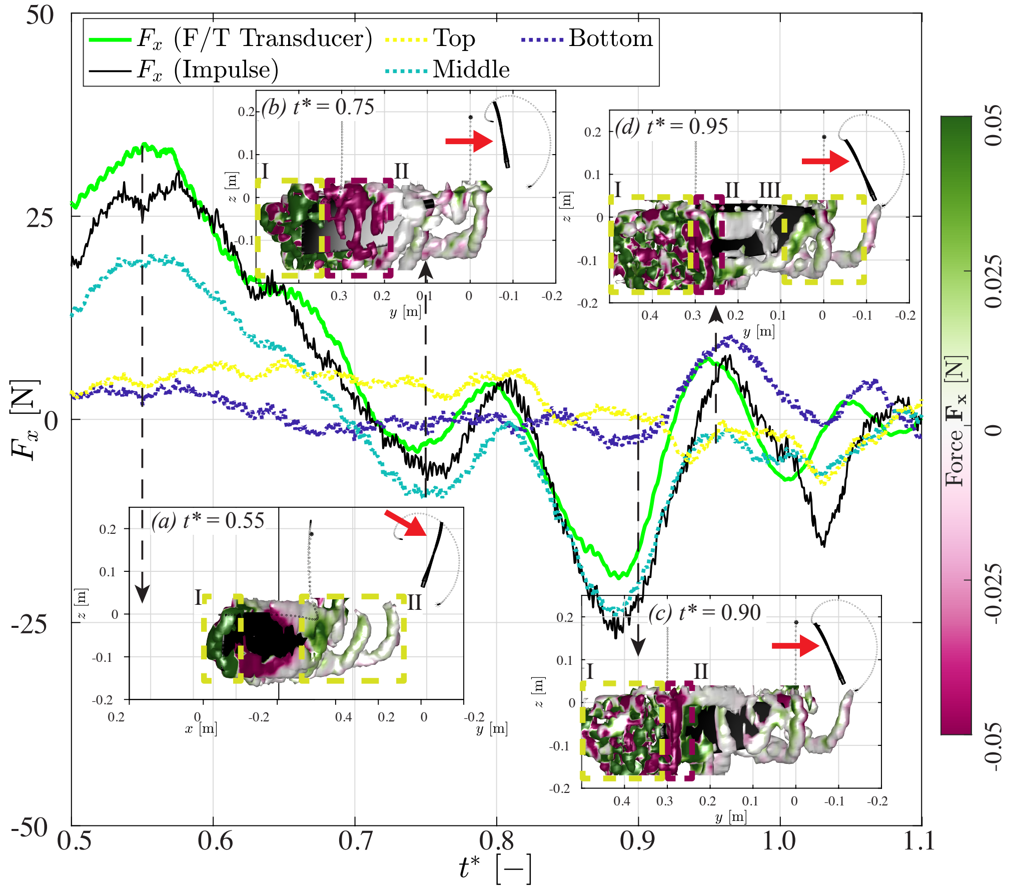

Figure 7. The propulsion force F_x for the Smoothie2 Plain Edge blade as a function of dimensionless time t^* during the second half of the stroke between $t^* = 0.5$ and $t^* = 1.1$. The propulsion force measured by the F/T transducer is shown in green. The general propulsion force reconstructed from the multi-layer impulse-based method is shown in black, with the force budget reconstructed from the flow at the top, middle and bottom of the blade is shown in yellow, cyan and blue, respectively. The insets at (a) $t^* = 0.55$, (b) $t^* = 0.75$, (c) $t^* = 0.90$ and (d) $t^* = 0.95$ show the iso-surface of $Q = 1 \times 10^{-5}\,\mathrm{s}^{-2}$ and the color represents the local contribution of propulsion force F_x. The main flow structure contributing to the propulsion force is marked by dashed rectangles and labeled by roman numerals. Inside of each inset, the viewing angle is indicated by a red arrow pointing at the top view of the blade at the same t^*.

component via the continuity equation. A 3D impulse-based method was then applied to estimate the propulsive component of the hydrodynamic force acting on the blade. Good agreement was observed between the propulsion estimated using the 3D impulse-based method and that measured directly with the force/torque transducer, supporting the validity of the approach. The 3D impulse-based analysis also enabled identification of the relationship between flow structures and propulsion throughout the stroke. Vortical structures near the lower edge of the blade were found to dominate during the initial 30% of the stroke. Between 30% and 75% of the stroke, propulsion is primarily generated by the leading-edge vortex. Beyond 75% of the stroke, the contribution to propulsion becomes predominantly negative.

REFERENCES

Adrian, RJ & Westerweel, J 2011 *Particle Image Velocimetry*. Cambridge University Press.

Baudouin, A & Hawkins, D 2004 Investigation of biomechanical factors affecting rowing performance. *Journal of Biomechanics* **37** (7), 969–976.

Caplan, N & Gardner, TN 2007 A fluid dynamic investigation of the big blade and macon oar blade designs in rowing propulsion. *Journal of Sports Sciences* **25** (6), 643–650.

Coppel, A, Gardner, TN, Caplan, N & Hargreaves, DM 2010 Simulating the fluid dynamic behaviour of oar blades in competition rowing. *Journal of Sports Engineering and Technology* **224** (1), 25–35.

Eldredge, JD & Jones, AR 2019 Leading-edge vortices: Mechanics and modeling. *Annual Review of Fluid Mechanics* **51** (Volume 51, 2019), 75–104.

Gehlert, P, Andreu-Angulo, I & Babinsky, H 2023 Vortex force decomposition—forces associated with individual elements of a vorticity field. *Experiments in Fluids* **64** (6), 112.

Grift, EJ, Tummers, MJ & Westerweel, J 2021 Hydrodynamics of rowing propulsion. *Journal of Fluid Mechanics* **918:A29**.

Jeong, J & Hussain, F 1995 On the identification of a vortex. *Journal of Fluid Mechanics* **285**, 69–94.

Kleshnev, V 2026 Efficiency of various blade types in rowing. *Sports Biomechanics* **0** (0), 1–11.

van Nieuwburg, WCAM, van Spreuwel, BJJ, Tran, MTK, Yang, MD, Greidanus, A, Mulder, G, Tummers, MJ, Westerweel, J, Suijker, W & van Wijk, R 2023 Improving rowing performance by adjusting oar blade size and angle. *Frontiers in Sports and Active Living* **5**, 1109494.